Application of the double paddle oscillator for quantifying environmental, surface mass variation

Haoyan Wei[1,2] and Joshua Pomeroy[1,*]

[1] Quantum Measurement Division, National Institute of Standards and Technology, Gaithersburg, MD 20899, USA

[2] Joint Quantum Institute, University of Maryland, College Park, MD 20742, USA

* To whom correspondence should be addressed.

E-mail: joshua.pomeroy@nist.gov

Phone: 301-975-5508

Fax: 301-417-0514

ABSTRACT

Sub-monolayer sensitivity to controlled gas adsorption and desorption is demonstrated using a double paddle oscillator (DPO) installed within an UHV (ultra-high vacuum) environmental chamber equipped with *in situ* film deposition, (multi)gas admission and temperature control. This effort is intended to establish a robust framework for quantitatively comparing mass changes due to gas loading and unloading on different materials systems selected or considered for use as mass artifacts. Our apparatus is composed of a UHV chamber with gas introduction and temperature control and *in-situ* materials deposition for future materials testing enabling *in situ* preparation of virgin surfaces that can be monitored during initial exposure to gasses of interest. These tools are designed to allow us to comparatively evaluate how different materials gain or lose mass due to precisely controlled environmental excursions, with a long term goal of measuring changes in absolute mass. Herein, we provide a detailed experimental description of the apparatus, an evaluation of the initial performance, and demonstration measurements using nitrogen adsorption and desorption directly on the DPO.

KEYWORDS

Double paddle oscillator, microbalance, instability of mass artifacts, gas adsorption and desorption

1. Introduction

The kilogram is the last of the seven base units of the international system of units (SI) which is based on a physical artifact instead of a fundamental physical constant. The present kilogram is defined as the mass of the international prototype of the kilogram (IPK), a cylinder made of Pt-Ir metal[1, 2]. However, physical artifacts change mass due to handling, surface oxidation, contaminant adsorption, and other chemical effects[3]. Similarly, each of the primary (and secondary, etc.) mass artifacts calibrated from the IPK are also subject to environmental variation so that the realized value of the kilogram is dependent on the history of these artifacts in the dissemination chain.

In an attempt to compensate for the accumulation of mass and "reset" mass artifacts, some national metrology institutes (NMIs) began using various cleaning methods prior to mass calibration. In 1989, a decision by the Comité International des Poids et Mesures (CIPM) was made to alter the definition of the kilogram to be the mass of the IPK after a standard BIPM (Bureau International des Poids et Mesures) "nettoyage-lavage" cleaning method: using a chamois cloth soaked in an equal parts mixture of ethanol and ether, the IPK is gently rubbed followed by washing in a jet of steam.[2, 4] While this method creates a significant (≈50 μg) immediate mass reduction, which depends primarily on the amount of contaminants present since last cleaning, the expectation was this would make a more reproducible standard after a short equilibration time. Unfortunately, the 3rd periodic verification performed between 1988 and 1992 measured a significant divergence in the mass of national prototypes with respect to the IPK. [2] These observations reinvigorated efforts to realize the kilogram through a fundamental physical constant by means of the Watt-balance[5-9] or the International Avogadro project[10-14]. While either approach would establish a time invariant definition of mass, dissemination to customers from this primary realization will continue to rely on physical artifacts susceptible to environmental effects, regardless of material selection, that require better understanding and control.

These environmental variations in mass artifacts have motivated studies by various surface analytical techniques, e.g., X-ray photoelectron spectroscopy (XPS) has revealed the chemical composition of the surface contaminants on artifacts[15-18]. While this has led to a greater

understanding of the composition of adsorbates, the kinetics and dynamics of the adsorption process is not understood well enough to explain the observed variations. Gravimetric methods, primarily by mass comparators or other type of balances, have measured mass variations due to environmental excursions involving water, organic vapor, air, and/or vacuum on different materials[19-22] by weighing the samples before and after exposure.[15, 16, 23] Most of these studies have been closely tied to the dissemination chain and, thus, performed on kilogram artifacts that can be difficult to manipulate or require exquisite sensitivity to detect adsorbate contributions at the molecular scale. Furthermore, mass variation studies under nominally ambient conditions make controlled environmental excursions difficult to execute and introduce uncertainties due to unintended, parasitic contributions that may be in the local environment. Additionally, previous work indicates that the macroscopic amount of contaminants is closely related to the microscopic chemical and physical processes during initial states that contribute to mass variation at very fast time scales,[24] which are difficult to examine and establish the time dependence in the ambient regime. A recent development at Federal Institute of Metrology (METAS) in Switzerland has demonstrated an instrument that combines a mass comparator, XPS, plasma cleaning, and storage within one system where the samples can be transferred between different sub-systems for measurements without breaking the vacuum.[16]

In order to develop a better understanding and minimize the effect of aggregating microscopic contributions to the mass, new measurements and better tools are needed to (*i*) establish a precise and predictive model of mass variation; and (*ii*) develop an engineering solution to minimize mass variation due to surface contamination. Ideally, a time-resolved, real time, surface sensitive, microweighing method is preferred in order to study the dynamic adsorption / desorption of gas molecules on candidate materials. Single crystal mechanical oscillators are promising candidates as microbalances that may capture the entire mass evolution induced by gas adsorption / desorption. One commercial example is the quartz crystal microbalance (QCM) used widely in industry and also implemented for monitoring the mass variation during and after plasma or UV/ozone cleaning at METAS.[17] Another example is the double paddle oscillator used in our work.

In this paper, we introduce an apparatus established at the National Institute of Standards and Technology (NIST) designed to quantify the microscopic contributions to mass variation that occur due to environmental excursions. Our objective is to create a versatile testbed capable of:

1) benchmarking gas adsorption and desorption against known measurements,

2) measuring uptake and release of environmentally common gasses on virgin and aged surfaces when exposed to well know temperatures and gas concentrations,

3) performing comparative studies of materials and coated surfaces for uptake and release susceptibility, and

4) developing an SI traceability link for sub-nanogram based oscillator techniques.

In order to do this, we have installed a high fidelity oscillator within an environmental chamber that allows control of the oscillator temperature with milli-Kelvin precision, the gas pressure and the gas composition. Additionally, we have installed the ability to deposit virgin coatings of different materials on the oscillator surface, which will be the subject of future work.

Critical to our strategy is the double paddle oscillator (DPO), implemented in our system as a sensor of mass variation due to surface processes, e.g., adsorption and desorption. The DPO was introduced by Kleiman, *et. al*[25, 26] and further significantly improved by the teams at Cornell and at the Naval Research Lab (NRL).[27-29] A photograph of a DPO similar to the one used in these measurements is shown in Figure 1b. Of the several observable mechanical modes, the 2nd anti-symmetric torsion mode (AS2) has a resonant frequency around 5.5 kHz (for a 300 μm thick DPO) and exhibits a very high quality factor (Q factor) on the order of 10^5 to 10^7, from room temperature down to about 4K.[28] Due to the high quality factor, the AS2 mode of the DPO is widely used in the scientific community for many different applications: the study of elastic properties of thin film materials,[30] detection of dynamical gravitational field generated by a mass,[31] and defect formation induced by ion-implantation.[32] Inspired by its ultra-sensitivity to mass loading, large surface area, and versatility, we demonstrate use of the DPO for the study of mass changes due to surface adsorption / desorption in the context of monitoring and stabilizing mass standards.

The content of the paper is organized as follows: we first describe the experimental setup of the DPO and relevant measurement electronics; then present some fundamental characteristics of the DPO including Q factor characterization (ring down measurements and frequency sweep) and frequency stability at room temperature; next, the dependence of temperature on the resonant frequency of the DPO are shown; next, the application of DPO to the measurements of nitrogen adsorption and desorption at cryogenic temperature; then, the mass sensitivity of the DPO is compared to the specifications of a commercial QCM and a mass comparator; and, finally, and the outlook of the DPO technique as an ultrasensitive mass metrology tool is outlined.

2. Experimental Section

2.1 Simple theory of oscillator based microbalances – QCMs and DPOs

Single crystalline silicon and quartz are best candidates for resonator materials due to their high materials purity and perfect crystal structures. These properties result in low internal losses and allow for excellent resonances with a very high intrinsic quality factor (Q factor). Quartz has been the most widely used resonator material since its piezoelectricity conveniently allows it to be used for both excitation and detection of the vibration. Some examples include 1) the miniature tuning forks employed as the timebase in watches and 2) microbalances used to measure small changes in mass during thin film deposition, electrochemistry, and for biosensing. For the convenience of the reader, we restate the basic theory for the QCM and the DPO.

In QCMs, the oscillation frequency depends strongly on the surface mass and Sauerbrey's equation allows one to obtain accurate measurements of mass change per area (Δm) as long as the frequency shift (Δf) is less than 2% of the unloaded resonant frequency[33]:

$$\Delta m = -\Delta f \frac{\sqrt{\rho_q G_q}}{2nf_R^{\,2}} \tag{1}$$

where ρ is density, G is shear modulus, n is the number of the harmonic, f_R is resonant frequency and the subscript "q" denotes quartz crystal. By comparison, the frequency shift in the DPO can be written as the following equation[34]:

$$\left.\frac{\Delta f}{f}\right|_{total} = \left.\frac{\Delta f}{f}\right|_{elastic} + \left.\frac{\Delta f}{f}\right|_{mass} = \frac{3G_{film}t_{film}}{2G_{sub}t_{sub}} - \frac{\rho_{film}t_{film}}{2\rho_{sub}t_{sub}} \tag{2}$$

where G is shear modulus, ρ is density, f is resonance frequency, and t is thickness of a film. The subscript "film" denotes films of gas molecules adsorbed onto the DPO surface and the subscript "sub" refers to the bare DPO with its metal electrode layer. In general, the total frequency shift can be attributed to two sources: (1) a change in the elastic properties, and (2) the mass loading of the materials deposited. Unlike crystalline solid films, the interaction within the films of adsorbed gas molecules is weak Van der Waals forces resulting in very small modulus. So, for our case, the elastic contribution is negligible (estimated to be <1%) and the frequency change is dominated by the mass loading on the DPO. As a result, equation 2 can be simplified to equation 3:

$$\left.\frac{\Delta f}{f}\right|_{total} \approx \left.\frac{\Delta f}{f}\right|_{mass} = \frac{\rho_{film}t_{film}}{2\rho_{sub}t_{sub}} \tag{3}$$

The linear mass-frequency relationship assumes the overlayer is tightly bonded to the substrate, which is assumed in this work. As we will see later, this is validated in the present measurements.

Excellent QCM systems are available in the marketplace, with frequency resolutions as high as 0.0035Hz with a fundamental resonant frequency typically in the 4.5 MHz to 6 MHz range. This precision corresponds to a film thickness resolution of 0.0043Å for a film density of 1 g/cm^3 or an areal mass resolution of 0.043 ng/cm^2. As we will show, our initial DPO results indicate a mass resolution as high as 0.027 ng/cm^2 at room temperature. As an advantage for application to mass standards, the DPO has a surface area of 6.65 cm^2, slightly less than 10% of the surface area for a Pt-Ir kilogram mass standard (72 cm^2) compared to the active surface area of QCM (0.5 cm^2). However, QCMs are able to operate in many diverse working environments, such as air and liquid.[27, 35] Therefore the QCM and

the DPO are both compelling instruments for addressing the diverse requirements of mass calibration and dissemination under various conditions.

2.2 DPO setup

Figure 1b shows a photo picture of an DPO fabricated from a commercial Si(100) wafer with gold electrode coating on one side. The DPO has a butterfly shape with head and wings connected by the narrow torsion rods called neck and leg. The DPO is supported at a nodal point by the bottom foot to create a rigid boundary condition so that the clamping loss is small. Finite element modeling reported in the literature identifies 8 Eigenmodes ranging from 0.1 kHz to 6 kHz.[27, 29] Of these vibration modes, the 2nd anti-symmetric mode (AS2) has the highest Q factor and is graphically depicted elsewhere[27, 36]. In the AS2 mode, the elastic energy is primarily stored around the neck region, which also has the largest strain occurring in the oscillation, and the leg remains at rest, minimizing the energy dissipation through clamping.

The DPO samples used in this demonstration were provided initially by the Naval Research Laboratory and their fabrication details are reported in previous papers.[27] The DPOs were made from high purity, undoped, float zone silicon (100) wafers (the resistivity is >10 kΩ·cm at room temperature) that are 300 μm thick and polished on both sides. Fabrication has now been reproduced at NIST for 300 μm and several other thicknesses. Unless stated otherwise, 300 μm is the default thickness used in this study.

In our current configuration, the DPO is excited and detected using capacitive coupling, which dissipates a minimal amount of energy into the DPO but requires high voltage to be effective (discussed further below). This implementation requires care to minimize cross-capacitance that can easily overwhelm the small coupling capacitance to the DPO. Other optical and mechanical approaches to drive and detect the DPO have also been reported.[31] Those approaches have the advantage to eliminate the high DC voltage present between the DPO and electrodes, and avoid the potential cross-capacitance issue, but may have the disadvantage of dissipating more energy into the DPO. We are comparing these methods in our lab and expect to report findings in a future publication.

The cryogenic vacuum assembly for mounting and driving (detecting) the DPO is shown in Figure 1c. The main structure is an OFHC (oxygen-free high conductivity) copper pedestal sitting on a round OFHC copper plate that mounts onto the cryogenic insert in the vacuum chamber. On the right side of the block is a dovetail assembly that allows the position of the Invar DPO clamp block (the gray block) to be precisely adjusted while maintaining a large contact area for thermal transport. The Invar alloy is used due to its uniquely low coefficient of thermal expansion (CTE), which is close to silicon (1.5 vs. 3, linear CTE $10^{-6}\cdot K^{-1}$)[37], and avoids the build-up of compressive stresses where the foot of the DPO is held due to material contraction upon cooling. (Since the measurements included here, we have successfully replaced the clamp block with an OFHC copper version that is much more efficient at cooling the DPO at low temperatures.) Beneath the wings of the DPO in the pedestal are two cylindrical pockets, which contain and shield the detect and drive electrodes (8 mm in diameter). The two pockets are completely separated and shielded from each other to avoid cross talk between the two electrodes and the entire copper pedestal is held at ground potential. The spacing between the DPO wings and two electrodes can be controlled by metal shim with a typical spacing of 150 μm. As a result, the calculated coupling capacitance is ~3 pF using a parallel plate model for one wing and electrode.

When the DPO mounting assembly is attached to the cryogenic insert, it is housed within a radiation shield inside the vacuum system schematically shown in Figure 1a. The UHV system has a typical base pressure on the order of $<10^{-7}$ Pa ($<10^{-9}$ Torr) at room temperature. The cryo-cooler system at the top of the vacuum chamber is a commercial "cryogen-free" cold finger installed into an exchange gas space that mechanically isolates the vacuum chamber from the vibration of the cold head operation. On the vacuum side of the sample stage, two cartridge heaters, a Si diode temperature sensor (heater sensor) and the DPO mounting assembly are mounted. A 2nd Si diode sensor (clamp sensor) is anchored on the Invar block to more closely monitor the sample temperature. The temperature is controlled by a PID (proportional-integral-derivative) closed loop using a commercial temperature controller. We also have a research-grade residual gas analyzer (RGA) for monitoring gas composition, precision leak valve connected to a multi-gas manifold, an optical lever arm detection scheme for comparison with the

capacitive method and a multi-pocket electron-beam evaporator for future *in-situ* materials deposition onto the DPO.

2.3 DPO excitation and measurement electronics

A schematic of the electronics setup used to drive and detect the DPO oscillation using the capacitive coupling approach is shown in Figure 2. Owing to the success and widespread use in the field, we have used essentially the same scheme as presented in Spiel, *et al*.[27] Starting at the upper left, each DPO wing and a corresponding copper electrode form a parallel plate capacitor. Following the "drive" leg, the electrostatic force on the DPO is described using the following equation:

$$F = CV^2/2d \tag{4}$$

where C is the capacitance between the DPO and the electrode (≈3 pF), V is the applied voltage and d is the spacing between the electrode and the DPO (≈0.15 mm). Both electrodes are biased by batteries to >200 VDC via 20MΩ resistors and isolated from the measurement electronics via isolation capacitors C1 and C2. The total voltage applied includes both static DC and the drive AC component:

$$V_{tot}^2 = [V_{DC} + V_{AC}\cos(\omega t)]^2 = V_{DC}^2 + 2V_{DC}V_{AC}\cos(\omega t) + V_{AC}^2\cos^2(\omega t) \tag{5}$$

Where ω is angular frequency, ω=2πf, f is frequency, t is time. When $V_{DC} = 0$, the first and second terms are zero and the resultant force has a frequency that is double the frequency of the applied voltage. However, if $V_{DC} >> V_{AC}$, the first term is static and the second term provides the greatest contribution so that force is at the same frequency as the applied voltage. In this way, a driving force is applied to the DPO from the frequency synthesizer or lock-in (with the switch in the figure in position 1 or 2, respectively.)

On the "detection side", the DPO oscillation causes a time varying capacitance, which causes a charge oscillation on C2. The changing charge on C2 is sensed as a current that is then converted to a voltage signal by current pre-amplifier with a typical sensitivity of 20 nA/V. This signal is then monitored by a frequency counter, lock-in amplifiers and an oscilloscope. For closed loop operation (self-excited) on a resonance, the output is amplified and phase shifted so that the lock-in's "signal

monitor" matches the synthesizer's phase and frequency. Then, the lock-in's sinusoidal output is used to excite the DPO and the drive will follow the oscillator's resonance frequency. To realize the high-Q performance, the instruments are synchronized with a rubidium timebase with an Allan variance less than 2×10^{-12} (100 seconds interval).

To initially locate the resonance frequencies, we sweep frequency from the synthesizer while monitoring the lock-in amplitude and phase. Once the frequencies of the major modes are located, the quality (Q) factors are measured by removing the driving force and measuring the 'ring-down,' i.e., decaying amplitude vs. time (the time constant τ can be >40 min at 4 K).

3. Results

3.1 Two determinations of quality factor - ring down measurements and frequency sweep

The sensitivity and stability of the DPO are both well characterized by the Q factor. Presented here are two complementary methods for measuring the value of the Q factor: (*i*) ring down (amplitude vs. time); and (*ii*) frequency sweep (amplitude vs. frequency). The Q factor is defined as $Q \equiv \pi\tau f_R$ where τ is time constant for the amplitude to decrease by a factor of e.

For the ring down measurement, the DPO is first placed in a self-excited loop for enough time so that the amplitude is a couple of orders of magnitude above the noise. Then the drive signal is removed to let the DPO ring down naturally while the amplitude is recorded with the lock-in. A ring down measurement at 297 K is shown in Figure 3 in a semi-log plot, where the function $B(t) = B_0\exp(-t/\tau)$ (red line) is fit to the data. In this example, the time constant is 11.07 s at a resonant frequency f_R = 5488.1886 Hz (measured separately by the frequency counter), which gives $Q = 1.91 \times 10^5$. Beyond 80 s the amplitude falls below 100μV (after a $>10^8$ V/A pre-amplification) and the measurement noise results in some scatter.

The second method to measure the quality factor is by scanning the frequency through the resonance and monitoring the amplitude. In this case, the DPO is excited with a fixed voltage by the frequency synthesizer. At each step, the frequency is held for a dwell time $\approx 10\tau$ to allow enough time for the DPO to reach steady-state amplitude. Figure 4 shows the amplitude and phase of the AS2 mode

during frequency sweep at room temperature. As expected, the phase changes by 180° and can facilitate rapidly locating the very narrow resonance frequencies. Fits to the phase and amplitude are an arctangent and Lorentzian-like function (respectively) and give f_R and τ [27, 36] from which the Q factor can again be calculated using $Q = \pi\tau f_R$. This method also yields $Q = 1.91 \times 10^5$ at room temperature, which is the same as from the ring down measurement. Generally, if Q is large ($>10^5$) the ring down method is best since Q can be accurately determined in 2 τ, which is much faster than the frequency sweep method. For smaller Q the frequency sweep works well since the relaxation time is short enough that the sweep can be done efficiently.

Since Q is a measure of energy loss rate, many parameters can affect its value, including the properties of the materials used for the oscillator, the boundary conditions such as the clamping approach,[27] measurement noise, the temperature (value and stability), and the oscillator geometry. When the oscillator is cooled to cryogenic temperatures that minimize the thermo-elastic losses,[38] we and other research groups[28] have successfully demonstrated that the Q factor for this oscillator improves by two orders of magnitude, e.g., we measure $Q = 1.13 \times 10^7$ at 12.77 K. In addition, our most recent efforts with a thicker wafers show an increased Q by a factor of 2 at room temperature and 8 at cryogenic temperature respectively. All these efforts imply the potential for further improvement of Q factor in micro-fabricated DPOs by exploring different thicknesses and geometries. Efforts to improve the DPO performance will also leverage the finite element modelling (FEM) to optimize the DPO geometry and facilitate the search for other oscillator designs.

3.2 Frequency stability and discrimination

Since the mass change is directly related to the shift of resonant frequency (similar to Eq. 1), excellent frequency stability is important to reaching the ultimate sensitivity to mass variation. Figure 5a shows the variation in temperature and corresponding frequency over a 2.5 hour period at a preset temperature slightly higher than room temperature. In this case, the cryocooler is off and the temperature is stabilized by a PID loop controlling two cartridge heaters. The temperature varies between 299.898 K and 299.901 K with the vast majority of samples falling within a 1 mK band. The corresponding AS2

resonance frequency is primarily confined within 5567.8600 Hz ± 0.0002 Hz or a 400 μHz band. The same frequency data is plotted as a histogram in Figure 5b for the initial 1.75 hours measurement time. The data are well fit with a Gaussian distribution (red line). The Gaussian fit values for the center position and full-width-half-maximum (FWHM) are 5567.8599682 Hz (standard error 5.5 x 10^{-7} Hz) and 181 μHz (standard error 1.3 μHz) respectively for this DPO. The margin of error ($|\pm\Delta f_{Err}|$) for center frequency at 95% confidence interval is 1.1 x 10^{-6} Hz, which is about twice the standard error. To detect a difference in the mass of a DPO at two substantially different times, the center positions of the two frequency distributions must be distinguishable. The ability to distinguish between two distributions is the frequency resolution which is related to the margin of error by the ratio of $\Delta f_{Err}/f_R$. For the data fit in Figure 5b, we obtain $\Delta f_{Err}/f_R = 1.97 \times 10^{-10}$ at 95% confidence interval mentioned above.

For monitoring dynamic processes, the frequency resolution given above would overestimate the accuracy since achieving that precision requires a large number of samples. So, for the short time frequency stability, we use the ratio of the width of the Gaussian in Figure 5b to the center frequency $\Delta f_{FWHM} / f_R = 3.25 \times 10^{-8}$. This quantity gives the confidence interval for any one data point corresponding to a 1 s averaging time. Below we will discuss how these frequency resolutions relate to mass sensitivity.

To determine the statistical contribution to the frequency distribution and optimize the length of measurement period, the standard error as a function of sampling time is plotted in Figure 5c. If the frequency resolution is limited by that statistical sampling, then as the measurement time increases, the standard error is expected to decrease as $t^{-1/2}$. At about 1.25 hours, it starts to level out, indicating that longer measurement time no longer provides benefit in reducing standard error. The plateau implies that there are other contributions present, which enlarge the distribution width at longer times. Determining the exact sources is challenging, but room temperature drift and measurement noise are possible contributing factors. As a result, 1 hour to 2 hours are typically selected in our present measurements for high resolution measurements.

3.3 Correlation between resonant frequency and temperature

To a good approximation, the DPO can be described as an ideal, harmonic oscillator whose resonance frequencies are related to the ratio of the elastic constant k and the mass m. The elastic constant k is mostly determined by Young's modulus, which is known to be a function of temperature. Specifically, the elastic constant of Si increases as temperature decreases and this material 'stiffening' leads to the increase of resonant frequency at low temperature. Additionally, the sensitivity of the resonance frequency to temperature means that temperature fluctuations result in frequency fluctuations. To characterize the dependence of the DPO resonant frequency on temperature, the DPO is placed in the self-excited loop and the resonant frequency and temperature are continually recorded while cooling (warming) to (from) cryogenic temperatures, respectively. The rate of temperature change is less than 100 mK/s for both processes.

Figure 6 shows the resonant frequency as a function of temperature from 300 K down to about 15 K. The black line shows the cooling down process, while the red line shows the warm-up process. The two lines do not exactly overlap with each other due to hysteresis caused by the poor thermal conductivity of the Invar block (the block has since been replaced with OFHC copper). The blue curve shows the 1st derivative of the cooling curve, which indicates the local sensitivity of the frequency to the temperature (note that the detailed structure is due to thermal latency and is not representative of the functional dependence). At around 300 K, the dependence of frequency on temperature is about 170 μHz/mK, which is consistent with the value reported previously.[31] At cryogenic temperature of about 15 K, the frequency becomes much less sensitive to temperature with a value lower than 10 μHz/mK.

The correlation between the resonance frequency and the temperature is also demonstrated by comparing fluctuations in the temperature with fluctuations in the resonance frequency. As shown in Figure 7a, the frequency deviates in the opposite direction as the temperature (note the temperature axis is inverted). The sensitivity of the frequency to temperature near room temperature is calculated to be ≈160 μHz/mK, which is consistent with that shown in Figure 6. To quantitatively demonstrate this correlation, a plot of frequency vs. temperature is shown in Figure 7b and the correlation coefficient using Pearson's product moment is calculated to be -0.97637. Unity means 100% correlation, while zero

means no correlation and the minus sign indicates the relationship is in an opposite direction. This emphasizes the importance of temperature control in achieving high frequency stability.

3.4 Gas adsorption and desorption measurements

In order to demonstrate the capabilities and sensitivities described above for monitoring or measuring mass changes, we have grown and evaporated thin films of inert gas ices onto the DPO at cryogenic temperatures. Once the ice is deposited and relaxed, the temperature is slowly increased in small steps while monitoring the rate of the frequency, and thus mass, changes. A partial example chronology of these experiments is shown in Figure 8. In Figure 8a, the bare DPO is initially at 8.9 K when at ≈2.78 hrs N_2 gas with pressure of 6.4 x 10 $^{-}$4 Pa (4.8 x 10^{-6} Torr) is introduced (blue line). The gas adsorption rate (R_{ads}) can be described as $R_{ads} = S \cdot F$, where S is the sticking coefficient (which is effectively unity the conditions used) and F is the incident molecular flux. According to the Hertz-Knudsen formula, the molecular flux has the following expression:

$$F = \frac{P}{\sqrt{2\pi M k_B T}} \tag{6}$$

where P is pressure, M is mass of one molecule, k_B is Boltzmann constant, and T is gas temperature. Therefore the adsorption rate remains constant under a specific gas temperature and pressure, corresponding to a constant rate of mass change, and, therefore, frequency change. This behavior is shown in Figure 8a as the black line. (It should also be noted that this data was taken with a 400 μm DPO, which has a higher resonance frequency and Q factor than discussed earlier in detail for the 300 μm DPO.) At ≈3.02 hrs the N_2 gas is pumped out of the chamber, terminating the growth of the ice and resulting in a constant mass and resonance frequency thereafter. While the adsorption qualitatively demonstrates the mass sensitivity, quantitative evaluation is hampered by inaccuracies in determining the local gas pressure and temperature at the surface of the DPO.

Quantitative evaluation can be performed by using the time-reversal process of desorption (sublimation), since the desorption rate (R_{des}) can be written in an Arrhenius form as shown in equation 7:

$$R_{des} = C \cdot \exp(-\frac{E_a}{k_B T_{DPO}}) \quad (7)$$

where E_a is evaporation activation energy (or enthalpy of sublimation), C is a constant a pre-exponential factor and T_{DPO} is the DPO temperature, which can be measured accurately. Similar to adsorption, the desorption rate will remain constant as long as the temperature is constant and the ice is not depleted. An example is shown in Figure 8b, where a zoom-in on one of several temperatures in a desorption sequence is shown. Initially, the DPO with nitrogen ice is at 24 K and the ice is desorbing slowly. At ≈5.75 hrs, T_{DPO} is increased to 24.5 K and, after an initial transient due to the small Young's modulus change, the rate of frequency change settles to a constant value (slope) greater than the 24 K slope. A similar 0.5 K increase in T_{DPO} is shown at ≈5.89 hrs. The full set of measured rates can then be plotted (not shown) in an Arrhenius form to extract E_a, which is the thermodynamic enthalpy of sublimation and is found to be (7.29 +/- 0.2) kJ/mol for this case. Unfortunately, the thermodynamic reference data for this temperature and pressure has a high relative uncertainty with the accepted value at 36 K: (6.9 +/- 4.7) kJ/mol from NIST Web Thermo Tables (WTT)[39]. Additional measurements of neon, argon, krypton, xenon, carbon dioxide, oxygen and water have also been completed and will be presented completely in a separate publication. Unfortunately these measurements also suffer from imprecise enthalpy of sublimation reference data at these temperatures, hampering precise calibration. Therefore, we plan to deposit and passivate solid metal films *in situ* to facilitate calibration by *ex situ* gravimetric comparison. However, using the frequency analysis above, we estimate our dynamic precision to be about 30 ng as we track the loading and unloading of the DPO in real time.

4. Discussion

In the previous sections, we have reported on the development of the DPO mass sensor system, its performance metrics and sensitivity to environmental stability. In section 3.4, we demonstrated the ability to monitor mass changes through adsorption and desorption; in this section we seek to evaluate the mass sensitivity and make a comparison to its closet instrumental sibling, the QCM.

In these measurements, the principal quantity of interest is the mass change, which is derived from the frequency shift using the relationship in equation 3. The absolute mass change $\Delta m = \rho V = \rho_{film} A t_{film}$, where A is the estimated surface area of DPO 6.65 cm^2. The mass change can then be written as $\Delta m = 2\ m_0\ (\Delta f/f_0) = 2\ \rho_{sub}\ t_{sub}\ A\ (\Delta f/f_0)$. For both the DPO and the QCM, the frequency resolution (uncertainty in Δf) determines the mass sensitivity.

Shown in Table 1 is a theoretical comparison between mass measurement instruments for the case of water adsorption. The DPO and research grade QCM have mass sensitivities one order of magnitude higher than standard QCM. The best QCM we found (research grade) in terms of mass sensitivity is Inficon IC6[40], which has an impressive areal mass sensitivity of 0.043 ng/cm^2. At present, our preliminary results demonstrate that the DPO's mass resolution is about 0.027 ng/cm^2, or 1.6 times better than IC6 at room temperature. Under the assumption of water condensation (molecule size is about 2.75Å in diameter[41]), this translates into less than one thousandth of monolayer coverage.

Comparing the specifications of the QCM and the DPO, the DPO has a larger active surface area (6.65 cm^2 vs. 0.5 cm^2). Although QCM has a surface area of 3.08 cm^2 (both sides), the majority of it is enclosed by the crystal holder and the open area for deposition is only about 0.5 cm^2. This area advantage of DPO (>10 times larger than QCM) makes it a better surface-sensitive instrument. However, the QCM operates at a higher frequency requiring less frequency precision for the same mass sensitivity. The QCM also utilizes a mechanical mode with minimal lateral displacement, which enables it to function reasonably well under atmospheric pressure conditions where gas damping becomes a problem for the DPO. Ultimately, we plan to perform studies with both instruments, which are expected to be complementary in bridging different temperature and pressure regimes.

In order to realize traceability to absolute mass, one calibration method being considered for both the DPO and QCM is to weigh them against traceable gravimetric standards before and after materials deposition. In general, the mass of the film deposited is much smaller compared to oscillators, e.g., a 100 nm thick film of gold deposited on one side of DPO will have a total mass loading of 0.64 mg (gold

density 19.3 g/cm^3), which should allow for a direct connection to traceable standards. Careful checks and controls have to be exercised to reduce uncertainty due to the environmental excursions in and out of the deposition chamber for these tests, but sufficient protocols appear possible.

One advantage of having this extreme mass sensitivity in a system with a large dynamic range in pressure and temperature is the capability to study adsorption dynamics in the sub-monolayer coverage regime. Starting from a clean surface, the adsorption process has two distinct regimes: 1) the adsorption is initially heterogeneous between gas molecules and the surface of mass standard materials until the contaminants cover the entire surface, then 2) the adsorption crosses over to an exclusively homogeneous process. Taking advantage of UHV pressures, this evolution can be dramatically slowed down, thus providing the time sensitivity to observe the detailed evolution. Detailed information of this type is critical not only for improving the current predictive models for mass variation, but also in the selection of promising materials for new mass standards as further explained in the following section.

Ultimately, the main objective for developing this new combined measurement, environmental control, and deposition capability is to perform comparative studies on the uptake and outgassing of different materials and/or coatings when exposed to common environmental gasses. By performing solid depositions *in situ*, we expect to measure total mass uptake for a given surface and compare that uptake to surfaces of different materials. Similarly, coatings that reduce uptake can be tested for efficacy and as well thermal cycling schemes that might allow for a reversible cleaning process.

While the ideal objective would be to identify a material or coating system that renders a mass artifact impervious to its environmental history, practically we can only hope to minimize the mass variation due to uptake and outgassing processes. To improve precision further, accurate predictive models must exist that are informed by the kind of detailed studies enabled by the DPO (and/or QCM) in this environmental chamber. This could lead to a method in which some recordation of a particular artifact's environmental history would be used to estimate a correction factor on a mass calibration, accounting for some uptake or loss and reducing the frequency with which comparative calibrations are required.

5. Summary

In this article, we describe the development of a Si double paddle oscillator in a wide range environmental chamber for the study of subtle mass variation due to gas molecule adsorption / desorption. This system has been designed to measure total mass changes due to environmental gas exposures on different materials systems or coating for selection of the best mass artifacts. With all systems installed, we have realized an instrumental performance that results in a mass sensitivity of 0.027 ng/cm^2, comparable to that of the best known QCM commercially available (0.042 ng/cm^2). We have demonstrated this capability by growing (evaporating) an N_2 ice while observing the linear change in the resonance frequency corresponding to the mass gain (loss).

Acknowledgement. The authors would like to thank Dr. Tom Metcalf at Naval Research Lab (NRL) for supplying part of DPO samples and helpful discussion with the initial experimental setup, as well as Dr. Neil Zimmerman at NIST for helpful discussion in cross-capacitance reduction.

REFERENCES

[1] Richard D 2003 The SI unit of mass *Metrologia* **40** 299-305

[2] Girard G 1994 The 3rd Periodic Verification of National Prototypes of the Kilogram (1988-1992) *Metrologia* **31** 317-36

[3] Davidson S 2003 A review of surface contamination and the stability of standard masses *Metrologia* **40** 324-38

[4] Girard G 1990 The washing and cleaning of kilogram prototypes at the BIPM *BIPM Monographie*

[5] Eichenberger A, Baumann H, Jeanneret B, Jeckelmann B, Richard P and Beer W 2011 Determination of the Planck constant with the METAS watt balance *Metrologia* **48** 133-41

[6] Steiner R L, Williams E R, Ruimin L and Newell D B 2007 Uncertainty Improvements of the NIST Electronic Kilogram *IEEE Trans. Instrum. Meas.* **56** 592-6

[7] Eichenberger A, Genevès G and Gournay P 2009 Determination of the Planck constant by means of a watt balance *Eur. Phys. J. Spec. Top.* **172** 363-83

[8] Robinson I A and Kibble B P 2007 An initial measurement of Planck's constant using the NPL Mark II watt balance *Metrologia* **44** 427-40

[9] Picard A, Hao F, Kiss A, de Mirandes E, Stock M and Urano C 2009 Progress on the BIPM Watt Balance *IEEE Trans. Instrum. Meas.* **58** 924-9

[10] Andreas B, Azuma Y, Bartl G, Becker P, Bettin H, Borys M, Busch I, Fuchs P, Fujii K, Fujimoto H, Kessler E, Krumrey M, Kuetgens U, Kuramoto N, Mana G, Massa E, Mizushima S, Nicolaus A, Picard A, Pramann A, Rienitz O, Schiel D, Valkiers S, Waseda A and Zakel S 2011 Counting the atoms in a Si-28 crystal for a new kilogram definition *Metrologia* **48** S1-S13

[11] Andreas B, Azuma Y, Bartl G, Becker P, Bettin H, Borys M, Busch I, Gray M, Fuchs P, Fujii K, Fujimoto H, Kessler E, Krumrey M, Kuetgens U, Kuramoto N, Mana G, Manson P, Massa E, Mizushima S, Nicolaus A, Picard A, Pramann A, Rienitz O, Schiel D, Valkiers S and Waseda A 2011 Determination of the Avogadro Constant by Counting the Atoms in a Si-28 Crystal *Phys. Rev. Lett.* **106** 030801

[12] Jörn S and Ernst O G 2012 The silicon route to a primary realization of the new kilogram *Metrologia* **49** L25-L7

[13] Picard A, Bignell N, Borys M, Downes S and Mizushima S 2009 Mass comparison of the 1 kg silicon sphere AVO#3 traceable to the International Prototype K *Metrologia* **46** 1-10

[14] Becker P 2003 Tracing the definition of the kilogram to the Avogadro constant using a silicon single crystal *Metrologia* **40** 366-75

[15] Davidson S 2012 Characterization of the long-term stability of mass standards stored in vacuum by weighing and surface analysis *Metrologia* **49** 200-8

[16] Fuchs P, Marti K and Russi S 2012 New instrument for the study of 'the kg, mise en pratique': first results on the correlation between the change in mass and surface chemical state *Metrologia* **49** 607-14

[17] Marti K, Fuchs P and Russi S 2013 Cleaning of mass standards: II. A comparison of new techniques applied to actual and potential new materials for mass standards *Metrologia* **50** 83-92

[18] Seah M P, Qiu J H, Cumpson P J and Castle J E 1994 Stability of Reference Masses II: The Effect of Environment and Cleaning Methods on the Surfaces of Stainless Steel and Allied Materials *Metrologia* **31** 93-108

[19] Mizushima S 2004 Determination of the amount of gas adsorption on SiO 2 /Si(100) surfaces to realize precise mass measurement *Metrologia* **41** 137-44

[20] Picard A and Fang H 2004 Methods to determine water vapour sorption on mass standards *Metrologia* **41** 333-9

[21] Schwartz R 1994 Precision Determination of Adsorption Layers on Stainless Steel Mass Standards by Mass Comparison and Ellipsometry: Part I: Adsorption Isotherms in Air *Metrologia* **31** 117-28

[22] Schwartz R 1994 Precision Determination of Adsorption Layers on Stainless Steel Mass Standards by Mass Comparison and Ellipsometry: Part II: Sorption Phenomena in Vacuum *Metrologia* **31** 129-36

[23] Gläser M and Borys M 2009 Precision mass measurements *Rep. Prog. Phys.* **72** 126101

[24] Fuchs P 2009 Low-pressure plasma cleaning of Au and PtIr noble metal surfaces *Appl. Surf. Sci.* **256** 1382-90

[25] Kleiman R N, Agnolet G and Bishop D J 1987 Two-level systems observed in the mechanical properties of single-crystal silicon at low temperatures *Phys. Rev. Lett.* **59** 2079-82

[26] Kleiman R N, Kaminsky G K, Reppy J D, Pindak R and Bishop D J 1985 Single-crystal silicon high-Q torsional oscillators *Rev. Sci. Instrum.* **56** 2088-91

[27] Spiel C L, Pohl R O and Zehnder A T 2001 Normal modes of a Si(100) double-paddle oscillator *Rev. Sci. Instrum.* **72** 1482-91

[28] Fefferman A D, Pohl R O and Parpia J M 2010 Elastic properties of polycrystalline Al and Ag films down to 6 mK *Phys. Rev. B* **82** 064302

[29] Liu X, Morse S F, Vignola J F, Photiadis D M, Sarkissian A, Marcus M H and Houston B H 2001 On the modes and loss mechanisms of a high Q mechanical oscillator *Appl. Phys. Lett.* **78** 1346-8

[30] White Jr. B E and Pohl R O 1995 *Elastic Properties of Thin Films* vol 356 p 567-72

[31] Haiberger L, Jager D and Schiller S 2005 Fabrication and laser control of double-paddle silicon oscillators *Rev. Sci. Instrum.* **76** 045106

[32] Liu X, Pohl R O, Crandall R S and Jones K M 1997 *Internal Friction in Ion-Implanted Silicon* vol 469 p 419-24

[33] Denison D R 1973 Linearity of a Heavily Loaded Quartz Crystal Microbalance *J. Vac. Sci. Technol.* **10** 126-9

[34] White B E, Hessinger J and Pohl R O 1998 Annealing and sublimation of noble gas and water ice films *J Low Temp Phys* **111** 233-46

[35] Borovsky B, Mason B L and Krim J 2000 Scanning tunneling microscope measurements of the amplitude of vibration of a quartz crystal oscillator *J. Appl. Phys.* **88** 4017-21

[36] Borrielli A, Bonaldi M, Serra E, Bagolini A and Conti L 2011 Wideband mechanical response of a high-Q silicon double-paddle oscillator *J Micromech. Microeng.* **21** 065019

[37] www.engineeringtoolbox.com.

[38] Houston B H, Photiadis D M, Marcus M H, Bucaro J A, Liu X and Vignola J F 2002 Thermoelastic loss in microscale oscillators *Appl. Phys. Lett.* **80** 1300-2

[39] http://wtt-pro.nist.gov/wtt-pro/.

[40] Certain commercial equipment, instruments, or materials (or suppliers, or software, ...) are identified in this paper to foster understanding. Such identification does not imply recommendation or endorsement by the National Institute of Standards and Technology, nor does it imply that the materials or equipment identified are necessarily the best available for the purpose.

[41] Zhang Y X and Xu Z J 1995 Atomic Radii of Noble-Gas Elements in Condensed Phases *Am. Mineral.* **80** 670-5

Figure captions

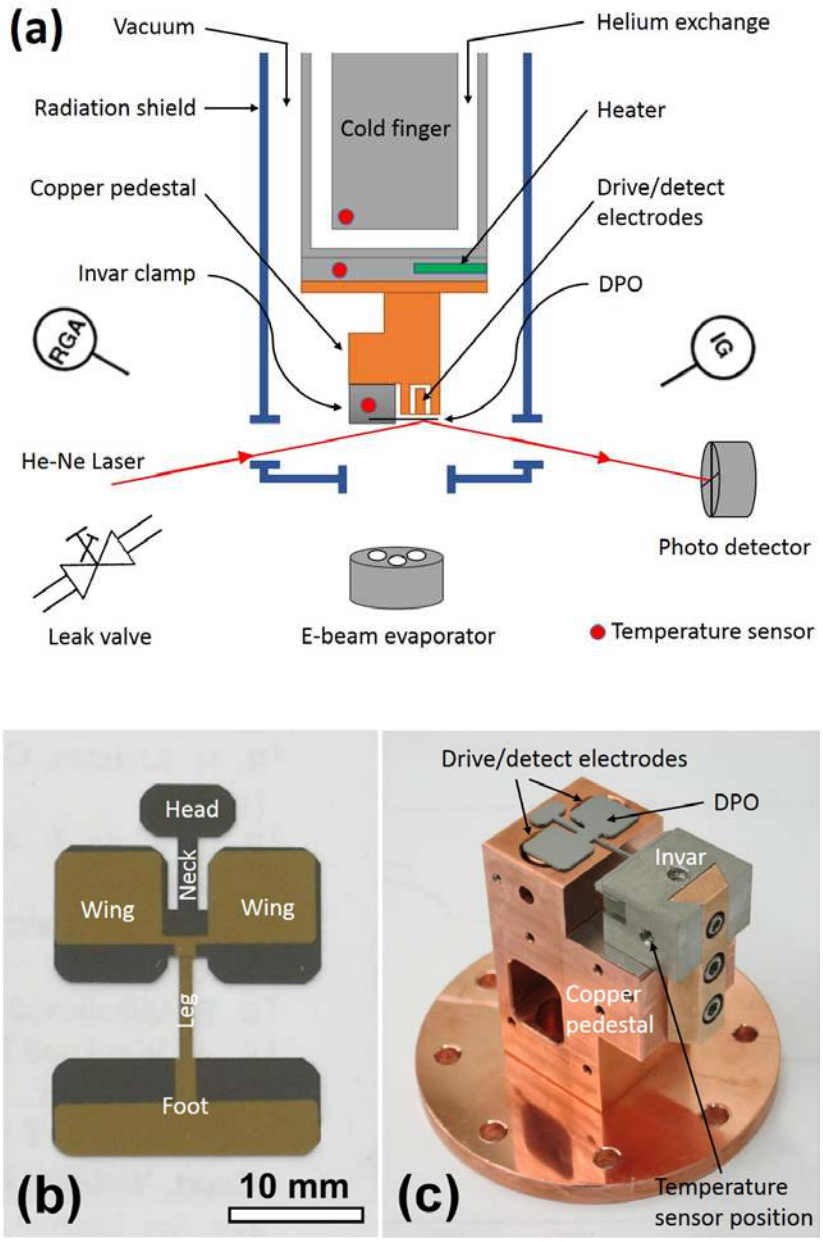

Figure 1. Schematic drawing of (a) the cryogenic vacuum system for monitoring environmental contributions to mass, (b) DPO geometry and dimension, and (c) the sample mount with a DPO assembled.

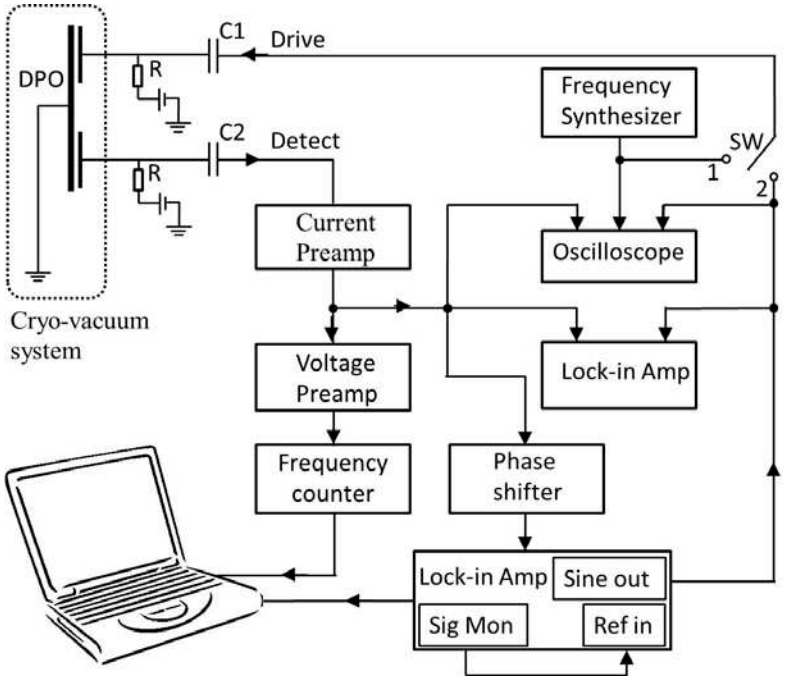

Figure 2. Schematic of the measurement system used to drive and detect DPO.

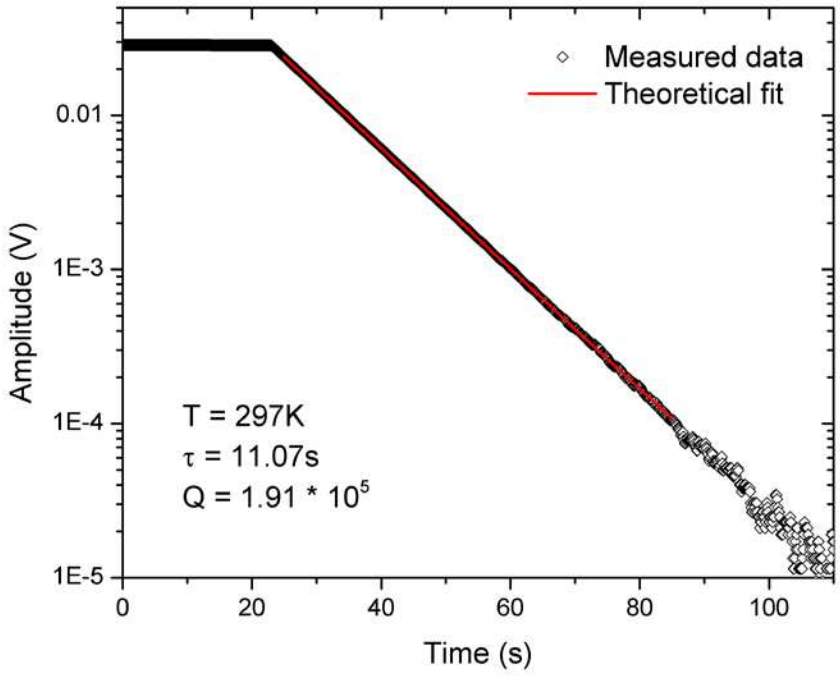

Figure 3. Undriven amplitude vs. time (ring down) measurement of the AS2 mode at room temperature. The diamonds are measured data, fitted with the theoretical model (red line). The resonant frequency is 5488.1886 Hz, the time constant from the fit is 11.07 s and the Q factor is 1.91 x 10^5.

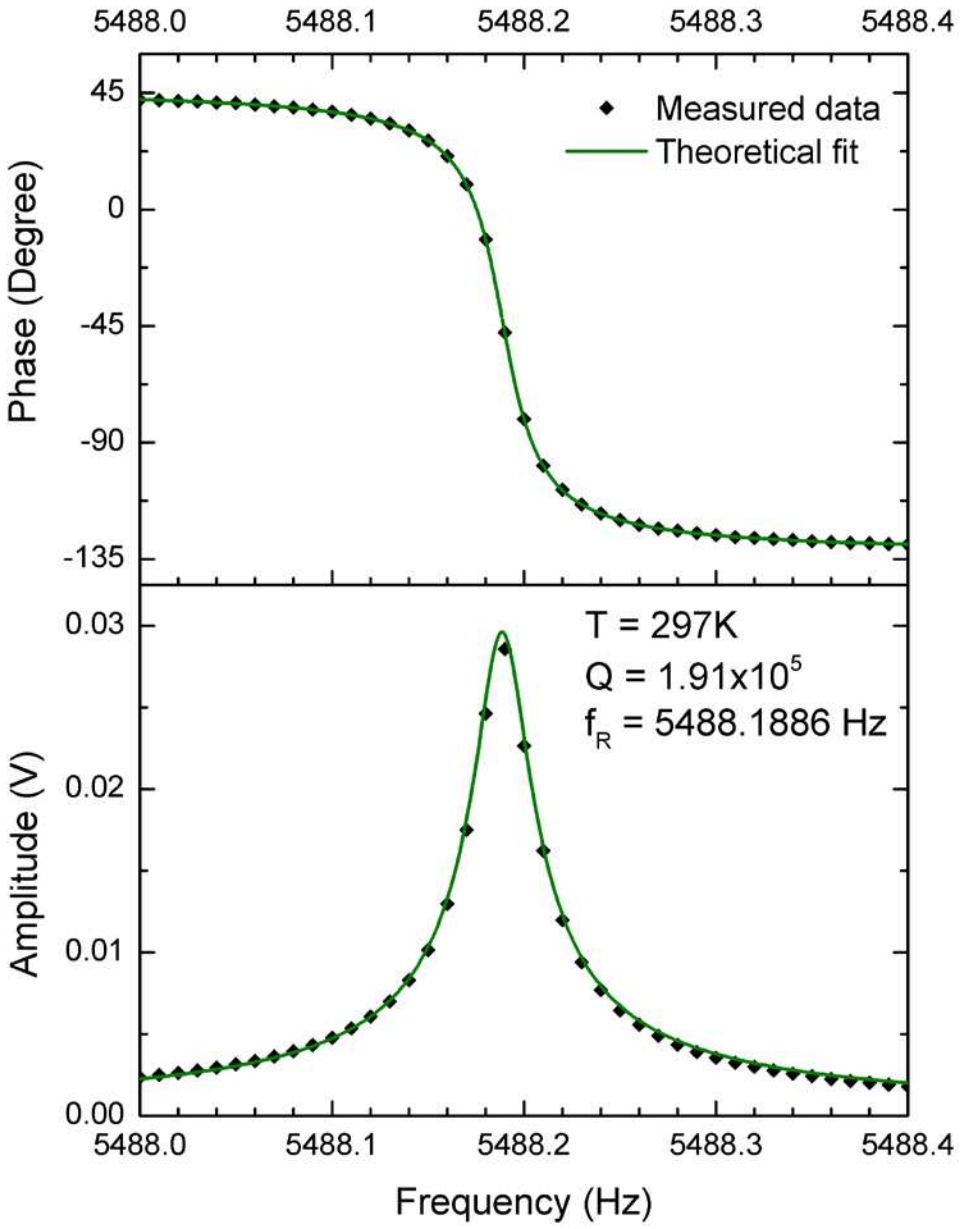

Figure 4. The amplitude and phase for a frequency sweep through the AS2 mode at room temperature are shown for the same DPO as in Figure 3. The diamonds are measured data. The green lines are theoretical fits of driven oscillators. The resonant frequency derived from the fit is 5488.1886 Hz. The Q factor calculated is 1.91 x 10^5, which is the value as obtained using the ring down method in Figure 3.

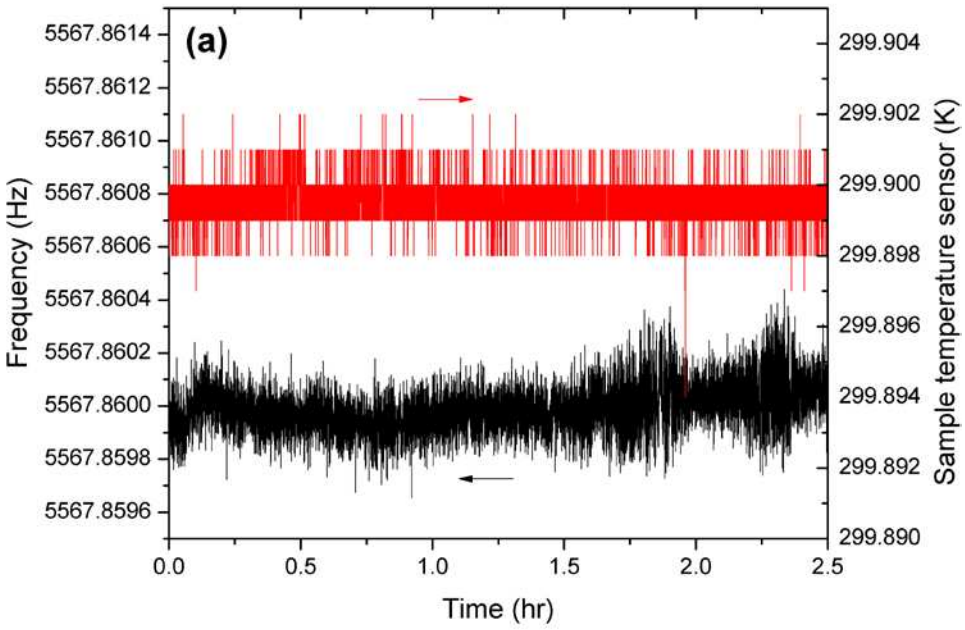
(a)
Frequency (Hz)
Sample temperature sensor (K)
Time (hr)
5567.8614
5567.8612
5567.8610
5567.8608
5567.8606
5567.8604
5567.8602
5567.8600
5567.8598
5567.8596
299.904
299.902
299.900
299.898
299.896
299.894
299.892
299.890
0.0
0.5
1.0
1.5
2.0
2.5

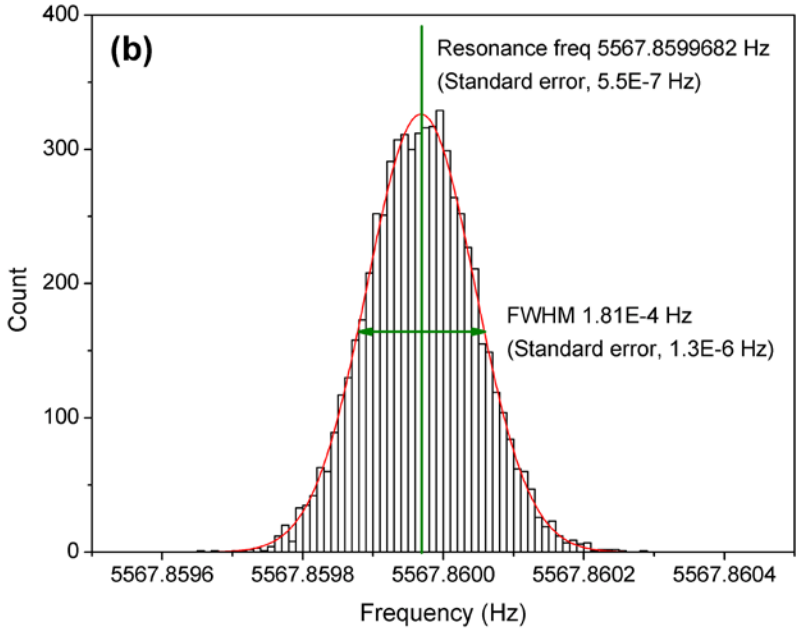
(b)
Resonance freq 5567.8599682 Hz
(Standard error, 5.5E-7 Hz)
FWHM 1.81E-4 Hz
(Standard error, 1.3E-6 Hz)
Count
Frequency (Hz)
400
300
200
100
0
5567.8596
5567.8598
5567.8600
5567.8602
5567.8604

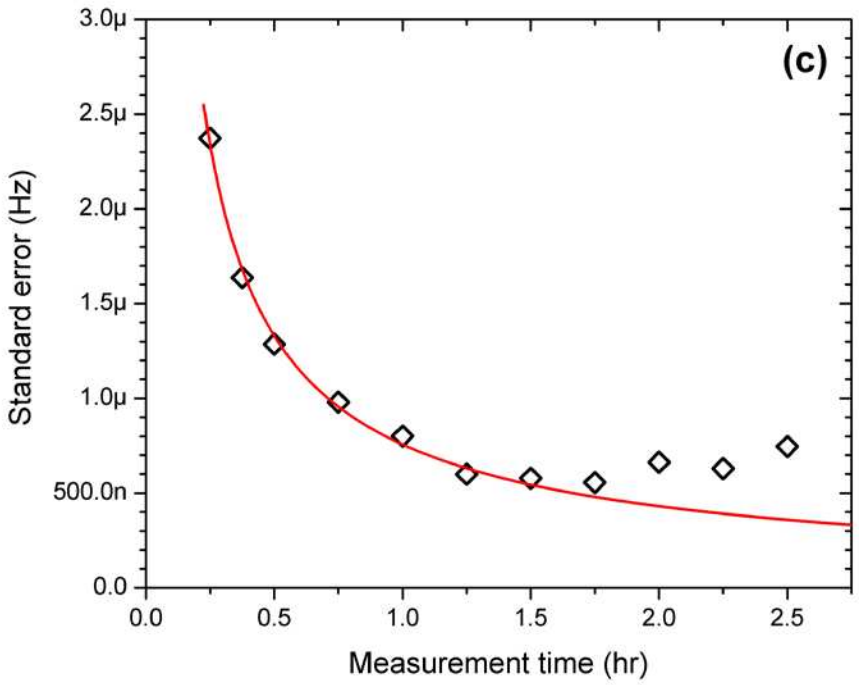

Figure 5. (a) Frequency and closed loop temperature data over a 2.5 hour period. The temperature varies primarily within 1 mK band and the corresponding frequency fluctuates within 5567.8600 ± 0.0002 Hz (gate time 1s). (b) The frequency histogram of the same data as in (a) for the initial 1.75 hours fitted with a Gaussian distribution (red line) with a center frequency is 5567.8599682 Hz and a FWHM of 181 µHz. (c) The standard error of the fitted resonant frequency decreases asymptotically with measurement time. At about 1.25 hours, a plateau is reached. The red line represents pure statistical uncertainty.

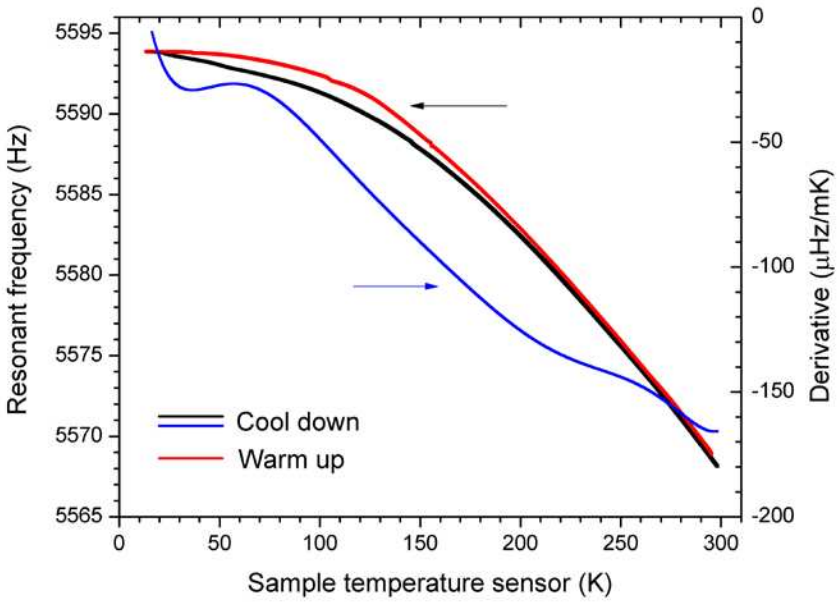

Figure 6. The shift of resonant frequency as a function of DPO temperature during initial cool down (black line) and subsequent warm up (red line) between room temperature and cryogenic temperature. The blue line shows the derivative of cooling down curve to reveal the local sensitivity of frequency to temperature, which at 300 K is about 170 μHz/mK (the difference between cool-down and warm-up is thermal latency).

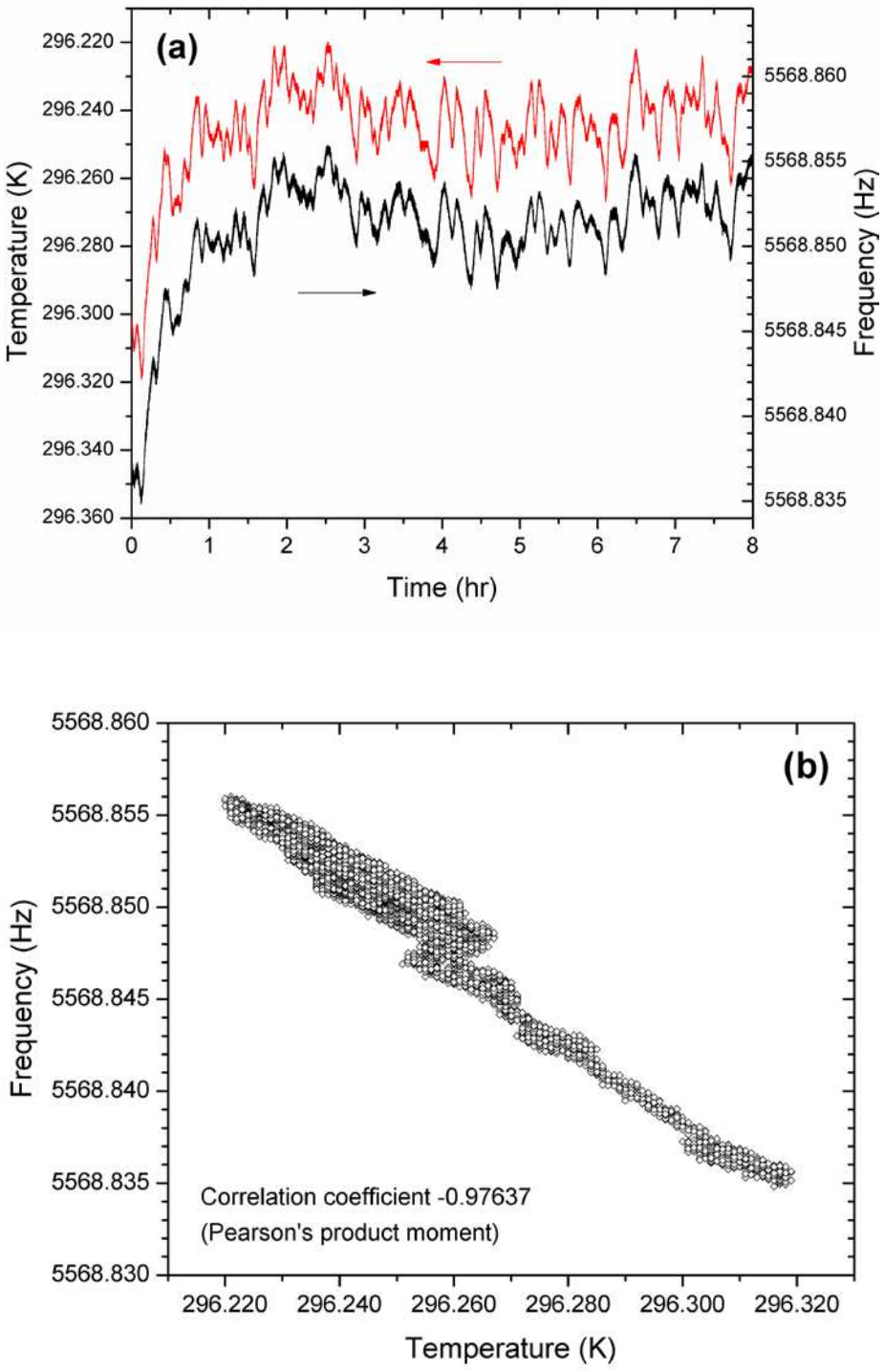

Figure 7. (a) The correlation of the resonant frequency with temperature shows the strong dependence of the two near room temperature. (b) The same data as (a) in a correlation plot; the correlation coefficient calculated from the plot is -0.97637, indicating a strong correlation.

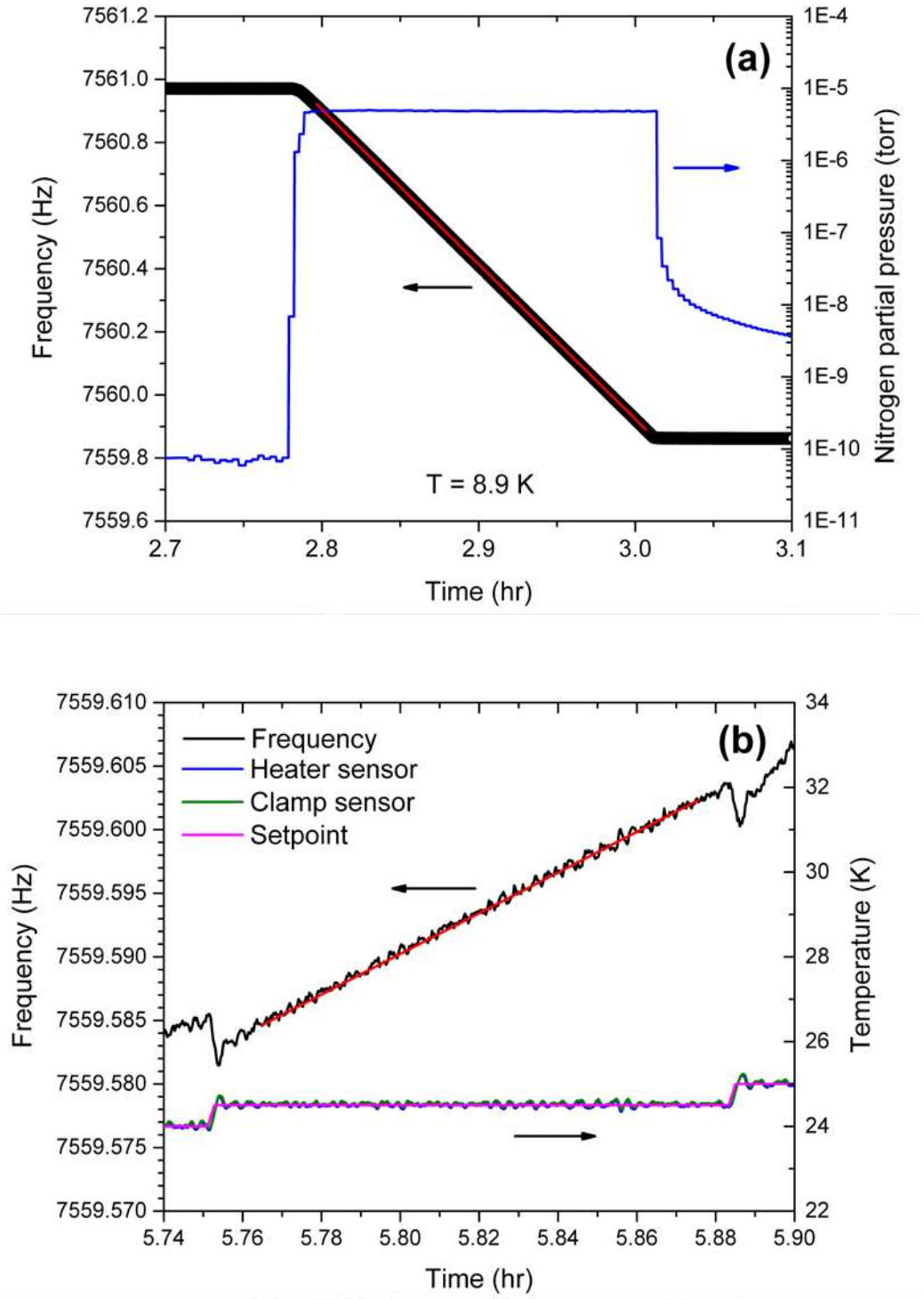

Figure 8. (a) Adsorption and (b) desorption measurements of nitrogen gas with DPO. The nitrogen film was first deposited at 8.9K under a partial pressure of 4.8 x 10^{-6} torr. Subsequently, it was evaporated isothermally at 24.5K. The red straight lines are arbitrary, indicating the linear change of frequency as a function of time.

Table 1. Comparison of microbalances and mass comparator at room temperature

	Resonant frequency (Hz)	Frequency resolution (Hz)	Surface area of both sides (cm^2)	Mass resolution		
				Absolute mass (ng)	Unit area (ng/cm^2)	Film thickness [c] (Å)
DPO (300 µm)	5 to 6 kHz (AS2)	1.1×10^{-6}	6.65 [a]	0.180	0.027	0.0027
Standard QCM (Inficon XTC/3)[40]	5 to 6 MHz	0.028	3.08 [b]	1.05	0.34	0.034
Research QCM (Inficon IC6)[40]	4.5 to 6 MHz	0.0035	3.08 [b]	0.132	0.043	0.0043
Mass comparator (Mettler Toledo M_One)[40]	/	/	/	100	1.4 (Pt-Ir kilogram)	0.14 (Pt-Ir kilogram)

[a] Foot clamping area is not included.

[b] The crystal diameter is 1.4 cm.

[c] Assumed film density 1 g/cm^3